Analysis on the inception of the magnetohydrodynamic flow instability in the annular linear induction pump channel

Zhao Ruijie
Research Center of Fluid Machinery Engineering and Technology,
Jiangsu University,
Zhenjiang 212013, China
e-mail: rjzhao@ujs.edu.cn

Dou Xiaohui
Research Center of Fluid Machinery Engineering and Technology,
Jiangsu University,
Zhenjiang 212013, China
e-mail: xiaohuidou11@163.com

Pan Qiang
Research Center of Fluid Machinery Engineering and Technology,
Jiangsu University,
Zhenjiang 212013, China
e-mail: pq91@qq.com

Zhang Desheng[1]
Mem. ASME
Research Center of Fluid Machinery Engineering and Technology,
Jiangsu University,
Zhenjiang 212013, China
e-mail: zds@ujs.edu.cn

B. P. M. (Bart) van Esch
Mem. ASME
Department of Mechanical Engineering,
Eindhoven University of Technology,
Eindhoven 5600MB, The Netherlands
e-mail: b.p.m.v.esch@tue.nl

Analysis on the Inception of the Magnetohydrodynamic Flow Instability in the Annular Linear Induction Pump Channel

Flow instability is the intricate phenomenon in the annular linear induction pump (ALIP) when the pump runs at off-design working condition. A three-dimensional (3D) numerical model is built to simulate the flow in the pump channel. The pump heads at different flow rates are accurately predicted by comparing with experiment. The simulation results show the fluid velocity is circumferentially nonuniform in the pump channel even at the nominal flow rate. The flow in the middle sector continuously decelerates to nearly zero with the reducing flow rate. Reversed flow occurs in the azimuthal plane, followed by vortex flow. The reason for the heterogeneous velocity field is attributed to the mismatch between nonuniform Lorentz force and relatively even pressure gradient. It is seen that the flow in the region of small Lorentz force has to sacrifice its velocity to match with the pressure gradient. An analytic expression of the axial Lorentz force is then developed and it is clearly demonstrated the Lorentz force could be influenced by the profiles of velocity and radial magnetic flux density. The coupling between velocity and magnetic field is studied by analyzing the magnitudes of different terms in the dimensionless magnetic induction equation. It is found the dissipation term is determined by not only the magnetic Reynolds number but also the square of wave number of the disturbance in each direction. The smaller disturbing wave number weakens the dissipating effect, resulting in the larger nonuniform magnetic field and axial Lorentz force.
[DOI: 10.1115/1.4050008]

1 Introduction

Liquid metals, such as sodium and lead-bismuth alloy, are prospectively used as the heat transfer fluid in the faster breeder reactors [1]. The high risk of liquid metal leakage and explosion requires for nonintrusive transporting technology. Electromagnetic pump, using induced Lorentz force to drive the liquid metal, has been employed in this field [2]. Annular linear induction pump (ALIP) has been received increasing attention in the last decades since it is superior to other pump types for being the nuclear coolant pump with the advantages of leakage free, low noise and vibration and easy maintenance [3]. However, the electromagnetic force in the pump channel could induce strongly unsteady flows as the designed flow rate increases, resulting in large fluctuations in the flux and pressure at the outlet and significant drop in the pump efficiency [4]. It is of great importance to maintain a sufficient pump efficiency in order to keep the energy consumption in acceptable level. Therefore, having a deep insight into the evoking mechanism of the flow instability becomes the critical issue for designing a large efficient ALIP system.

Initial design of ALIP was developed at small flow rate. Since 1980s, large ALIPs appeared in Russian, France, and Germany [5] and the flow instability became a challenge for pursuing larger flow rate. Then, much work has been focused on understanding the mechanism of the flow instability in ALIP's environment. Gailitis and Lielausis [6] found a critical condition for occurring unsteady flow in ALIP was $\mathrm{Rm}\cdot s > 1$, where Rm is the magnetic Reynolds number and s is the slip velocity. Kirillov and Karasev proved the criteria in a real ALIP [7]. They found low frequency fluctuations in the measured flow rate and pressure, accompanied by the nonuniform distributions of velocity and magnetic field in the azimuthal direction. Meanwhile, Araseki et al. [8] studied the double-supply frequency (DSF) pressure fluctuation of an ALIP applied with low frequency current. The unstable pressure was attributed to the cutting off of the induced magnetic field at both ends of the pump channel. To suppress the fluctuation, they proposed to arrange grading windings (gradually decreasing winding number) at both ends in order to reduce the end effect [9]. Araseki et al. [10] further studied the low frequency pressure pulsation and found the cause of the fluctuation, by means of a simplified numerical simulation, was the presence of unstable large vortices in the azimuthal plane of the pump channel. They proposed to change the current phase order in windings to reduce the local Lorentz force and have a better control of the flow pattern in the channel [11].

Due to the lack of visualization technique in the ALIP test, it is difficult to observe the internal flow and magnetic fields, as well as the interaction between each other. Numerical modeling provides the mean of studying the complex magnetohydrodynamic (MHD) flow in the pump. In fact, in Araseki et al.'s work [10], a simple two-dimensional (2D) numerical model was built to simultaneously solve the Navier–Stokes equation and the magnetic induction equation. The simulated curve of developed pressure difference versus flow rate agreed well with the experimental data only in a narrow range around the nominal flow rate, and the large

[1]Corresponding author.

Contributed by the Fluids Engineering Division of ASME for publication in the Journal of Fluids Engineering. Manuscript received September 8, 2020; final manuscript received January 24, 2021; published online March 4, 2021. Assoc. Editor: Moran Wang.

discrepancy between two results at low and moderate flow rates was attributed to the failure of 2D model in modeling three-dimensional (3D) flow phenomena in the pump. Kirillov and Obukhov [12] developed a similar 2D model to study DSF fluctuation and internal vortices in ALIP. A numerical model based on time harmonics finite difference method was created by Lee and Kim [13], and they studied some important characteristics of the ALIP, such as eddy current, DSF pressure pulsation, and Lorentz force under various flow rates. Zhao et al. [14] created a 2D model to study the effects of different winding schemes on both the pump performance and the internal flow.

In recent, the modeling of ALIP has been realized in 3D model by coupling the flow and electromagnetic fields [15]. Asada et al. [2,16] used a commercial computational fluid dynamics (CFD) software combined with a homemade electromagnetic solver to simulate the ALIP performance in a three-dimensional (3D) coupling model. The developed pressure difference in the simulation results agreed well with the measurements in the corresponding prototype. Reversed flow and vortices were observed in both the meridian and azimuthal planes. Although their results demonstrated the variation in velocity can influence the induced magnetic field and finally change the Lorentz force and the flow pattern, the mechanisms for occurring such flows is still ambiguous. The direct numerical simulation was carried out in a dimensionless 2D model representing the meridian plane of ALIP and a wide range of Rm and Ha numbers were studied in terms of the flow pattern [4,17]. The literature review has shown that 3D numerical modeling of the MHD flow in ALIP is still scarce due to the complex coupling processes. The reasons for flow instability and the correlations among the coupled physical parameters have yet to be deeply revealed.

In this work, a 3D numerical model is built based on the dimensional information of an ALIP in Ref. [10]. The description of the numerical model and model settings is presented in Sec. 2. The model validation by comparing the simulated pump differences with the experimental data is presented in Sec. 3, as well as the visualizations of steady and unsteady flow patterns in the pump channel. The mechanism for occurring the unstable flows is analyzed and discussed in Sec. 4. The conclusions are summarized in Sec. 5.

2 Description of the Numerical Model

2.1 Geometrical Model. In order to overcome the limitations of 2D ALIP model, a 3D physical model was created to consider the nonuniformity in the flow and electromagnetic fields, as well as the resulting unsteady flows. The detailed pump dimensions and operating parameters can be found in Ref. [10]. The 3D physical model of the ALIP is shown in Fig. 1(*a*), and the schematic of the simulation model is shown in Fig. 1(*b*). The physical model represents a 1/8 section of the ALIP prototype. The modeled domain contains two 1/2 outer stators. That is to, say, there are eight individual outer stators circumferentially surrounding the pump channel and the space between two adjacent outer stators is filled with air. Figure 1(*c*) is the model cross section viewed from the pump axis (z direction). It can be seen that each of the half outer stator occupies a space with 30 deg in the azimuthal direction and the air gap between two outer stators takes up 15 deg. The dimensions of main modeled components are presented in Fig. 1(*d*). Since the main focus in this work lays in understanding the mechanism of MHD flow instability rather than pump performance prediction, the zone occupied by windings and slots was simplified to compromise the confliction between the required computational cost and the complex 3D geometry. Trivial structures, such as coil slots and stator teeth, are not represented. The original 36 winding slots and teeth are replaced by the subdomain 2 as a whole in Fig. 1(*b*), where a tuned current density is azimuthally imposed to stimulate the magnetic field in the pump channel to reach the same level as the prototype's measurement. The average amplitude of magnetic flux density is 0.08 T in the middle of the channel when no liquid metal runs in the ALIP. The inner stator is integral. In addition, the stainless steel ducts are considered in the model while the originally narrow air gap between the outer duct and winding is ignored. The air domain surrounding the ALIP's components is shown as the transparent zone in Fig. 1(*b*). The simulation is assumed in the isothermal condition and thus, the energy equation is deactivated.

Although the unstable flows may occur in the form of large scale vortex that can extend through the whole perimeter of the channel [2,10], the sectional model is defined in this work due to the heavily required computational time and resources because the mesh required for solving fluid flow should be fine enough to resolve the near-wall region while the mesh required for solving electromagnetic field needs small aspect ratio. It is the limitation of this model that the vortex flow with large scale (normally occurring at low flow rate) over the circumferentially modeling length cannot be simulated. However, the authenticity of the numerical model could be well validated by comparing the predicted results with the experimental data at relatively high flow rates, at which the unstable flows occur merely in small scale, as presented in Sec. 3.1. Moreover, the influence of the modeling circumferential length on the disturbance in the induced magnetic field and the resulting Lorentz force is deeply studied in the part of mathematic analysis presented in Sec. 4. The mechanism of the occurrence of unstable flows in different circumferential lengths of the modeling domain is revealed.

2.2 Governing Equations and Model Settings. The numerical model is consisted of two parts. The liquid sodium in the pump channel is incompressible and the flow field is described by the conservative equations of mass and momentum, which are expressed as

$$\nabla \cdot \boldsymbol{u} = 0 \tag{1}$$

$$\frac{\partial \boldsymbol{u}}{\partial t} + (\boldsymbol{u} \cdot \nabla)\boldsymbol{u} = \nabla \cdot \left(-\frac{p}{\rho} + \nu \left[\nabla \boldsymbol{u} + (\nabla \boldsymbol{u})^T \right] \right) + \frac{\boldsymbol{F}_{lz}}{\rho} \tag{2}$$

where ρ is the flow density, $\boldsymbol{u}$ is the velocity vector, and p is the pressure. $\nu = \nu_f + \nu_T$, ν_f and ν_T are the fluid viscosity and turbulent viscosity. $\boldsymbol{F}_{lz} = \boldsymbol{J} \times \boldsymbol{B}$ is the induced Lorentz force, where $\boldsymbol{J}$ and $\boldsymbol{B}$ are the current density and magnetic flux density. The set of equations is applied only in the liquid domain. The turbulence is modeled using the standard k–ε model and the coupling between turbulence and electromagnetic field is ignored. From the practical viewpoint, the current model can predict the main flow characteristics, as long as the magnetic Reynolds number is below or only slightly exceeds one [12,18].

The electromagnetic field is solved using the set of Maxwell equations in the A–Φ formulation. The equations of Ampere's law and the current continuity are expressed as

$$\frac{1}{\mu}[\nabla \times (\nabla \times \boldsymbol{A}) - \nabla(\nabla \cdot \boldsymbol{A})] + \sigma \left(\frac{\partial \boldsymbol{A}}{\partial t} + \nabla \Phi - \boldsymbol{u} \times (\nabla \times \boldsymbol{A}) \right) = \boldsymbol{J}_e \tag{3}$$

$$\nabla \cdot \left(\sigma \frac{\partial \boldsymbol{A}}{\partial t} + \sigma \nabla \Phi - \sigma \boldsymbol{u} \times (\nabla \times \boldsymbol{A}) - \boldsymbol{J}_e \right) = 0 \tag{4}$$

where $\boldsymbol{A}$ is the magnetic vector and satisfies $\boldsymbol{B} = \nabla \times \boldsymbol{A}$. μ is the magnetic permeability and σ, the electric conductivity. The Coulomb gauge $\nabla \cdot \boldsymbol{A} = 0$ is integrated by using the second term in Eq. (3) for the $\boldsymbol{A}$ convergence [19]. Φ indicates the electric potential. $\boldsymbol{J}_e$ is the imposed external current density, if applied in the domain. The term $\sigma \boldsymbol{u} \times (\nabla \times \boldsymbol{A})$ in both equations is the induced current due to the motion of conducting fluid. The flow velocity $\boldsymbol{u}$ is coupled with the results of the fluid solver. The set of equations is applied in the whole domain. In the nonconducting zones, such

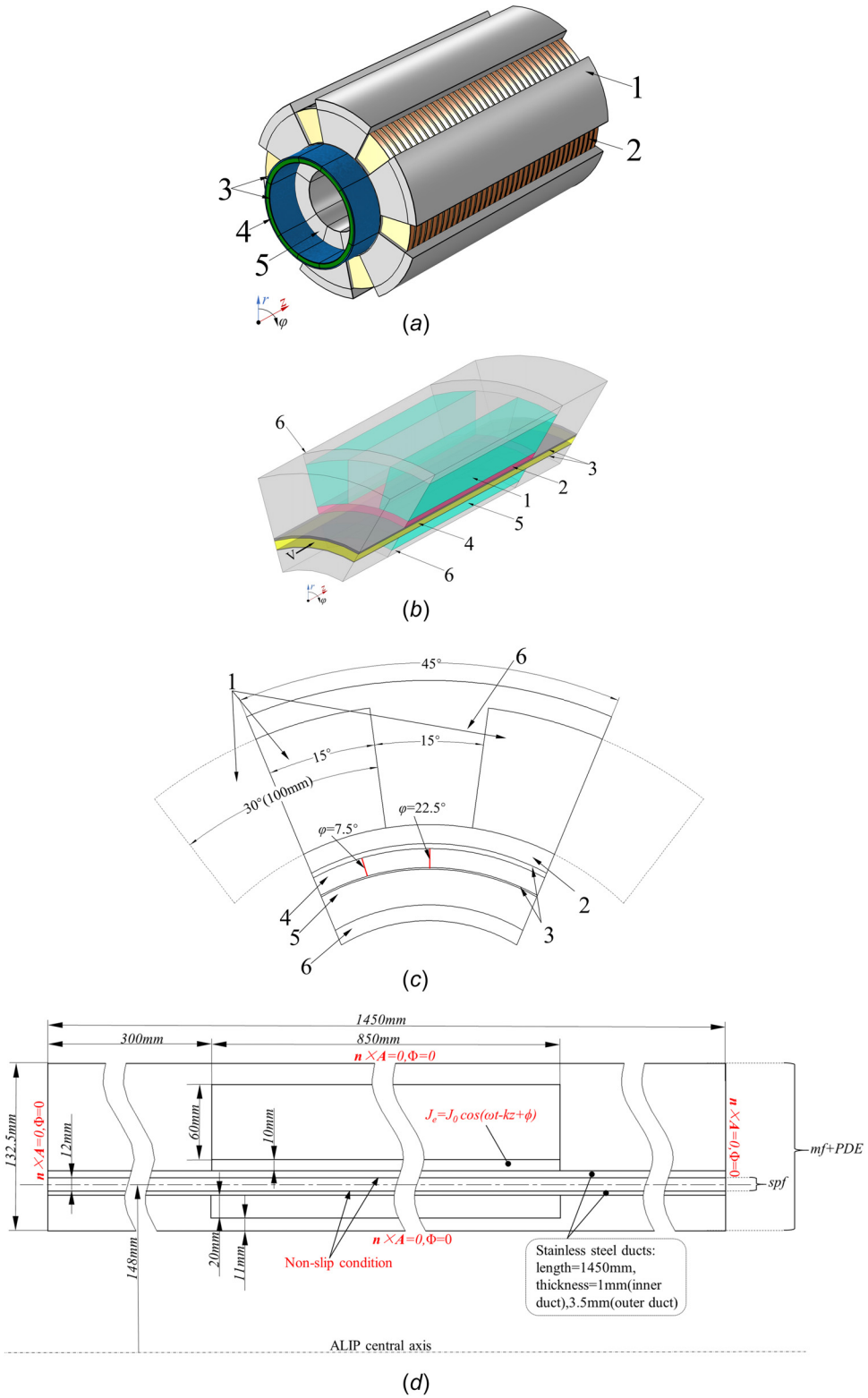

Fig. 1 (*a*) Three-dimensional physical model of the ALIP, (*b*) schematic of the 1/8 simulated model of the ALIP prototype, 1-outer stators, 2-windings (they are represented by a conductor with the externally applied current density Je in (*b*)), 3-stainless steel ducts, 4-liquid sodium in pump channel, 5-inner stator (integrated), 6-air domains, (*c*) cross-sectional view of the pump model, and (*d*) meridian view at $\varphi = 7.5$ deg of the pump model and the dimensions of main components

as the stators, simplified winding zone and air zones, the electric conductivity is zero and the part of velocity-induced current is not solved in the governing equations. In the conducting zones, such as liquid sodium and metal ducts, the full form of Eqs. (3) and (4) is solved. $\boldsymbol{J_e}$ is applied in the simplified coil zone as the external current density.

The above equations were discretized and solved in the software COMSOL 5.2 based on the finite element method. COMSOL provides a magnetic field solver (magnetic field interface, or mf interface) to calculate Eq. (3). However, the Coulomb gauge and velocity-induced current are not available in the solver. The weak forms of the two added terms were derived and defined in the solver. In addition, the potential Φ was introduced in Eq. (3) using a self-defined Lagrange multiplier. The equation of current continuity was solved by defining the corresponding weak form of Eq. (4) in the partially differential equation (PDE) interface in COMSOL, which provides an interface to solve the user-defined PDE. The Lagrange multiplier defined in the mf interface was set as the solved variable and shape function of the user-defined PDE to enforce the divergence free of current density and thus, closing the set of equations. Quadrant order was used in the shape function. The edge element method was used to solve the magnetic vector by default.

2.3 Boundary Conditions. The material properties are summarized in Table 1. The effect of magnetic hysteresis on ferromagnetic materials is very marginal in such device (0.3% difference in the prediction by Abdullina and Bogovalov [20]) and therefore, the relative magnetic permeability of the stators is set as 1000. In order to help the solution convergence, the electric conductivity of the nonconducting zones is defined as 1 S/m and therefore, the full form of Eqs. (3) and (4) were solved in the whole domain. As shown in Fig. 1(*d*), the magnetic insulation condition ($\boldsymbol{n} \times \boldsymbol{A} = 0$) and $\Phi = 0$ are defined on all external boundaries of the surrounding air domain. A current density in the form of $J_e = J_0 \cos(\omega t - kz + \phi)$ was defined in the winding zone to represent the external three phase current, where ω indicates the input current angular frequency, k is the wave number, and ϕ is the phase angle. The wave number is calculated as $k = \pi/\tau$, where τ is the pole pitch. The equivalent current density magnitude $J_0 = 1.27 \times 10^7$ A/m^2 was azimuthally imposed in the winding zone to achieve the same level of induced magnetic flux density as that in the prototype measured in the centerline of channel height without liquid metal in the channel.

The liquid sodium zone was simulated using the CFD solver (single-phase flow interface, or spf interface) in COMSOL, which is based on the Reynolds-averaged Navier–Stokes formulation. The standard wall function was applied on the channel wall, considering the high Reynolds number. The Lorentz force was calculated from the results of the solved electromagnetic field in the modified mf interface. A uniform velocity profile determined by the simulated flow rate was defined at the inlet of the channel and zero pressure was imposed at the outlet with 1 atm as the reference pressure. Nonslip condition was assumed on the channel walls and the wall roughness is 50 μm.

The scheme of the coupling calculation is presented here. The flow field was first calculated in a steady-state condition without the Lorentz force, and then the electromagnetic filed was simulated in a steady-state condition by introducing the fluid velocity obtained in the first step. In the third step, the flow field was recalculated in the steady-state condition by introducing the induced Lorentz force, which were calculated from the result of the second step. This iterative procedure was performed for five steps, and then both fields were coupled to simulate in the transient condition. In the transient solver, the segregated solver was chosen to iteratively calculate the spf interface and the mf + PDE interfaces. The solver for spf is PARDISO while GMRES and Multigrid solvers were used for mf + PDE. Since the backward differentiation formula was used in the transient solver, COMSOL will automatically adapt the time-step and a maximum time-step of 0.0004 s was defined to limit the time stepping too fast. The total simulation time is 1 s, which corresponds to 50 current cycles.

Table 1 Material properties and physical parameters used in the model

Parameters	Values
Sodium density (kg/m^3)	898.25
Sodium conductivity (S/m)	7.3×10^6
Sodium dynamic viscosity (Pa·s)	4.23×10^{-4}
Relative magnetic permeability of stator	1000
Relative magnetic permeability of air and sodium	1
Current frequency (Hz)	50
Pole pitch (m)	0.14
Stator length (m)	0.85
Pump channel width (m)	0.012
Mean radius of the cylindrical channel (m)	0.148
Winding type	Y

Table 2 Mesh independent study

Parameters	Mesh #1	Mesh #2	Mesh #3	Maximum relative error
Degree-of-freedom	2,113,252	3,726,607	5,232,458	
Δp (Pa)	−416,837	−417,408	−416,655	0.18%
B_r (T)	0.081050	0.081055	0.081005	0.06%
F_z (N/m^3)	−539,720	−539,980	−537,540	0.45%

2.4 Grid Verification. Mesh independence was studied by comparing the simulated results from the meshes with different numbers of control volume. The coarser mesh has 27,000 elements and 2,113,252 degrees-of-freedom while the finer one has 90,000 elements and 5,232,458 degrees-of-freedom. Table 2 presents the comparison of different monitored parameters. The results of steady-state simulation at $Q = 7.0$ m^3/min were used for the comparison. Δp denotes the pressure difference between two points located at the center of the pump channel (i.e., $r = 0.148$ m and $\varphi = 22.5$ deg) at $z = 0.95$ and $z = -0.1$ m. The radial magnetic induction B_r and the axial volume force F_z are taken from the point located in the middle of the channel (i.e., $r = 0.148$ m, $\varphi = 22.5$ deg, and $z = 0.425$ m). It is seen that the maximum relative errors are marginal among three meshes for all the monitored parameters and the moderate mesh #2 was used in the following simulations, as shown in Fig. 2. The thickness of the first layer of the grid is 0.0002 m and the corresponding wall y^+ value is 150.

3 Simulation Results

3.1 Annular Linear Induction Pump Performance Prediction and Validation. The numerical model was validated by comparing the Δp–Q curve of the numerical results with the

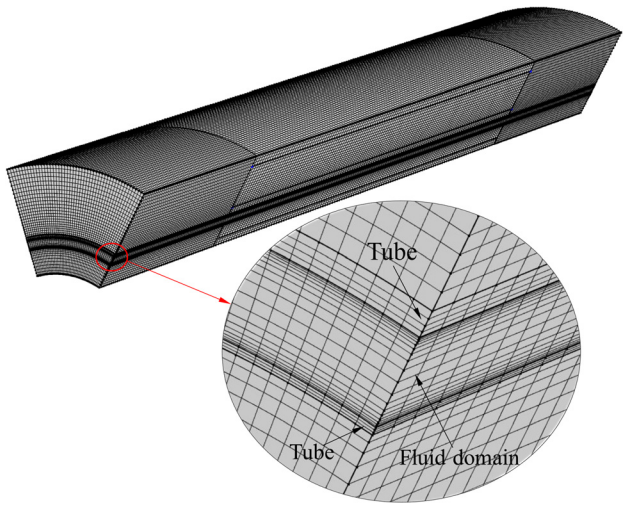

Fig. 2 Schematic of the computational mesh

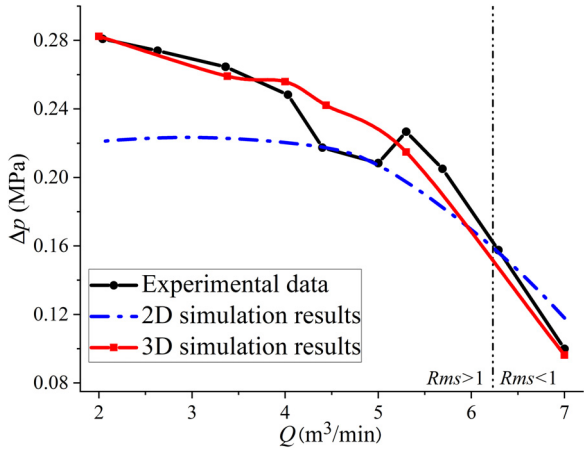

Fig. 3 Comparison of the Δ*p*–*Q* curve between the numerical models and experiment

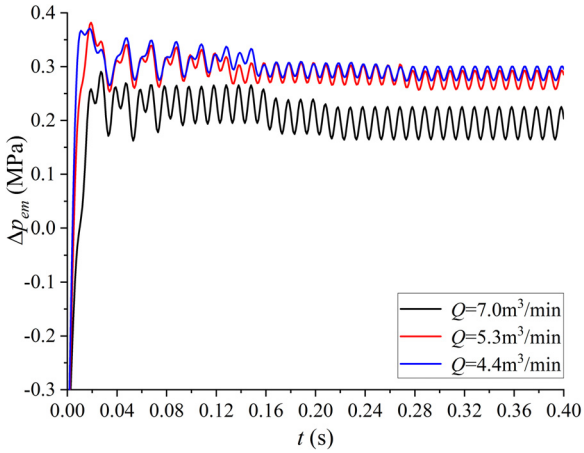

Fig. 5 Transient pressure difference between inlet and outlet of pump

experimental data [10], as shown in Fig. 3. The black solid line represents the experimental measurements while the blue dot dash line is the numerical results from their simplified 2D model. The solid line with the square mark illustrates the numerical results from the current 3D model. The curve was interpolated from six simulated flow rates ($Q = 2.0$, 3.4, 4.0, 4.4, 5.3, 7.0 m^3/min). It should be noted that the pressure difference Δp in the experiment included the local pressure losses in the nonelectromagnetic pipes and associated bends while the values of the numerical results are the pressure difference between the inlet and outlet of the electromagnetic section. According to the information presented in Figs. 11 and 27 of Ref. [10], where the pressure loss can be figured out at 7.0 m^3/min by the ratio of the measured pump difference Δp to the pressure increment in the electromagnetic section Δp_{em}. The corresponding pressure loss at other flow rates can be approximately estimated because the pressure loss is proportional to the flow kinetic energy or the square of the average flow velocity in the pump channel. Therefore, the presented 3D simulation results in Fig. 3 are corrected by subtracting the pressure losses due to pipe and bend. It can be seen that the Δp–Q curve predicted by 2D model can only agree with the experimental result around the nominal flow rate. However, the curve of the current 3D model agrees well with the experimental curve in the full range of tested flow rates.

The simulated pump efficiency is also calculated as $\eta = \frac{\Delta pQ}{3UIP_f}$, where U, I, and P_f denote the phase voltage, the phase current, and the power factor, which is determined by the phase shift between voltage and current. The simulated efficiency versus flow rate is presented in Fig. 4. The testing pump efficiency from the experiment in Ref. [11] is also presented for comparison. It is seen that the simplified model underestimates the efficiency at high flow rates while overestimating it at low flow rates. This error could be attributed to the simplification of the winding zone, which changes the total input power. A complete model with the windings accurately represented, slots and teeth were also created in the same mathematic formulation and used to simulate the pump performances at $Q = 5.3$ and 7 m^3/min. The corresponding efficiencies are also illustrated in Fig. 4 and the good match with the experiments validates the numerical model. To reduce the computational burden, the simplified model was used in the following simulations unless another model is specified.

The pressure difference between the inlet and outlet of pump electromagnetic section Δp_{em} at $Q = 7$, 5.3, 4.4 m^3/min is illustrated in Fig. 5. It demonstrates that after the startup time, the pressure difference fluctuates periodically with a cycle time of 0.01 s whose frequency is equal to two times the input current frequency, i.e., DSF. The time-averaged axial Lorentz force along the pump length is shown in Fig. 6. The Lorentz force increases as the flow rate decreases and the plateau of the Lorentz force occurs earlier at smaller flow rate. Negative Lorentz force appears at both ends indicating the common ending effect. The common phenomena in ALIP will not be analyzed further in this work since the readers can refer to the detailed discussions elsewhere [8,9].

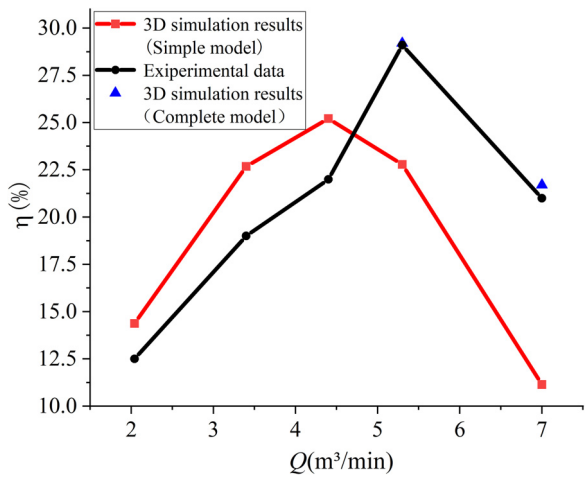

Fig. 4 Pump efficiencies at different flow rates from the simulations and experiments

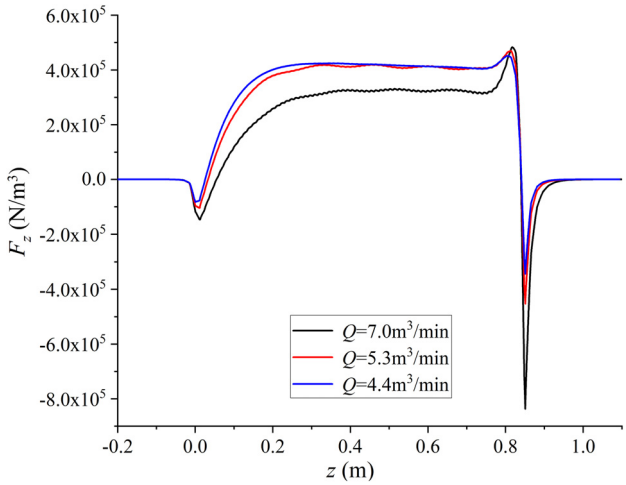

Fig. 6 Time-averaged axial Lorentz force in the pump longitude direction

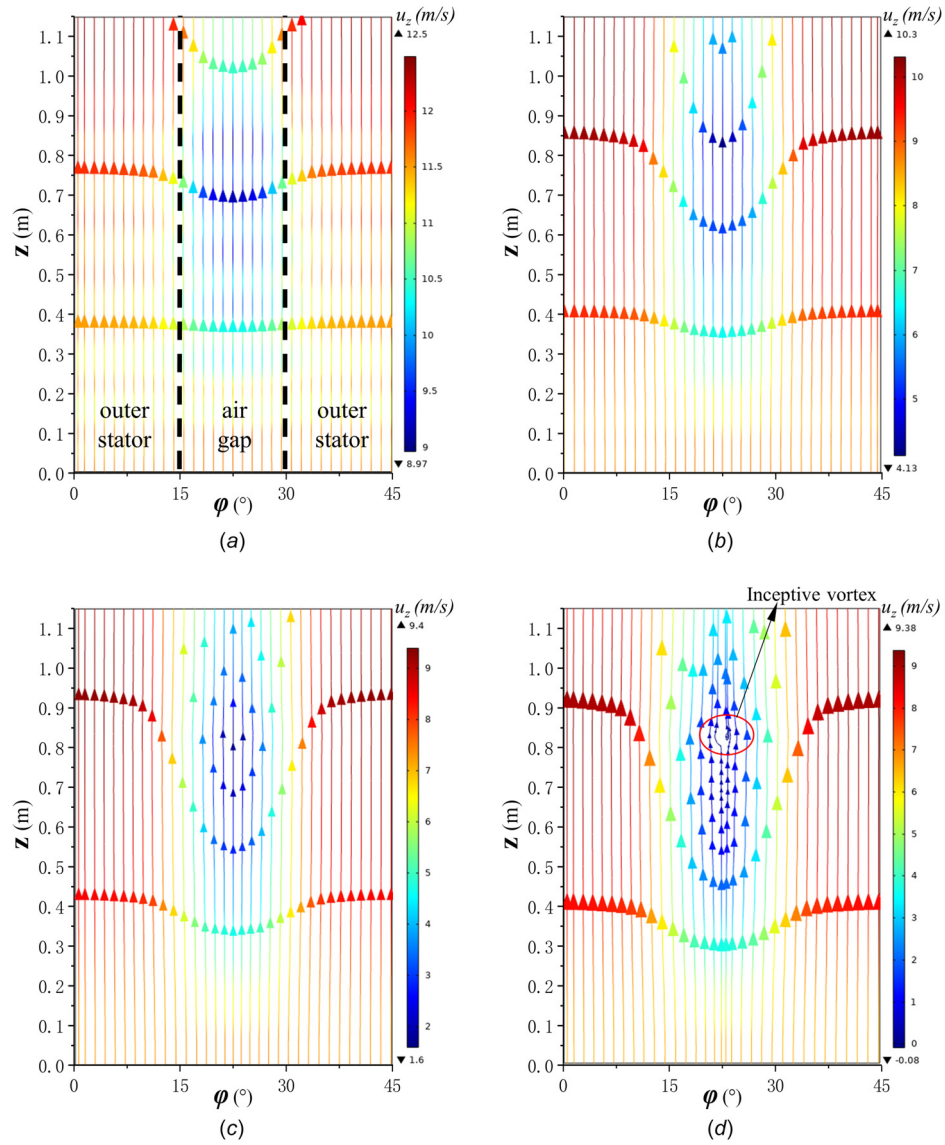

Fig. 7 Flow streamlines in the φ–z plane ($r = 0.148$ m) at (*a*) 7.0 m^3/min, (*b*) 5.3 m^3/min, (*c*) 4.4 m^3/min, and (*d*) 4.0 m^3/min

3.2 Flow Structures in the Pump Channel

3.2.1 Flow Structures Viewed From the φ–z Plane. The visualization of flow structure in the pump channel is of importance to understand flow instability. Although the flow structures in the pump channel typically possess 3D features, they are, respectively, visualized and analyzed in the created φ–z and r–z planes. For the transient cases, the first ten cycles are required to develop the stimulated magnetic field well in the pump channel. A φ–z plane is created at $r = 0.148$ m, which is located in the center of the channel along the radial direction. The flow streamlines in this plane are depicted and colored by the axial velocity magnitude under different flow rates.

When the flow rate was simulated between 7.0 and 4.0 m^3/min (approximately 60% of the nominal flow rate), the MHD flow can maintain relatively stable in the pump channel after the initially adapted time of about ten current cycles and the flow structures share some common features. Figures 7(*a*)–7(*d*) show the streamlines and axial component of the velocity in the φ–z plane of $r = 0.148$ m at four flow rates when the flow is stable. In order to identify the positions of outer stator and air gap outside of the pump channel, their projected areas in the φ–z plane of pump channel are depicted in Fig. 7(*a*). The flow enters the pump electromagnetic section ($z = 0$ m) with a uniform azimuthal profile. As the flow goes downstream, the velocity profile in the azimuthal direction becomes nonuniform, even at the nominal flow rate $Q = 7.0$ m^3/min. The flow in the middle sector ($\varphi = 15$–30 deg) of the pump channel always slows down while the flow in two lateral sectors ($\varphi = 0$–15 deg and 30–45 deg) speeds up. The lower the flow rate is, the larger the nonuniformity of the velocity profile in the azimuthal direction is. When the flow rate drops down to 4.0 m^3/min, the flow velocity in the middle sector decreases to nearly zero before leaving the electromagnetic section and a flickering vortex occurs near the outlet of the electromagnetic section, as seen in Fig. 7(*d*). Based on the observed flow field, the critical flow rate should be at some point between 4.0 and 4.4 m^3/min for occurring unstable flow in the pump.

When the flow rate further reduces, the flow in channel loses stable pattern and more complex flow structures are observed in the pump. Figures 8(*a*)–8(*c*) show the evolving flow streamlines in the φ–z plane at 3.4 m^3/min (approximately 50% of the nominal rate) and Fig. 8(*d*) shows the flow streamlines at 2.0 m^3/min in an instant when the flow is evolved long enough. As shown in Figs. 8(*a*)–8(*c*), a large vortex occurs in the middle of the electromagnetic section ($z = 0.52$ m) after the flow undergoes the developing stage. The vortex periodically evolves in three different

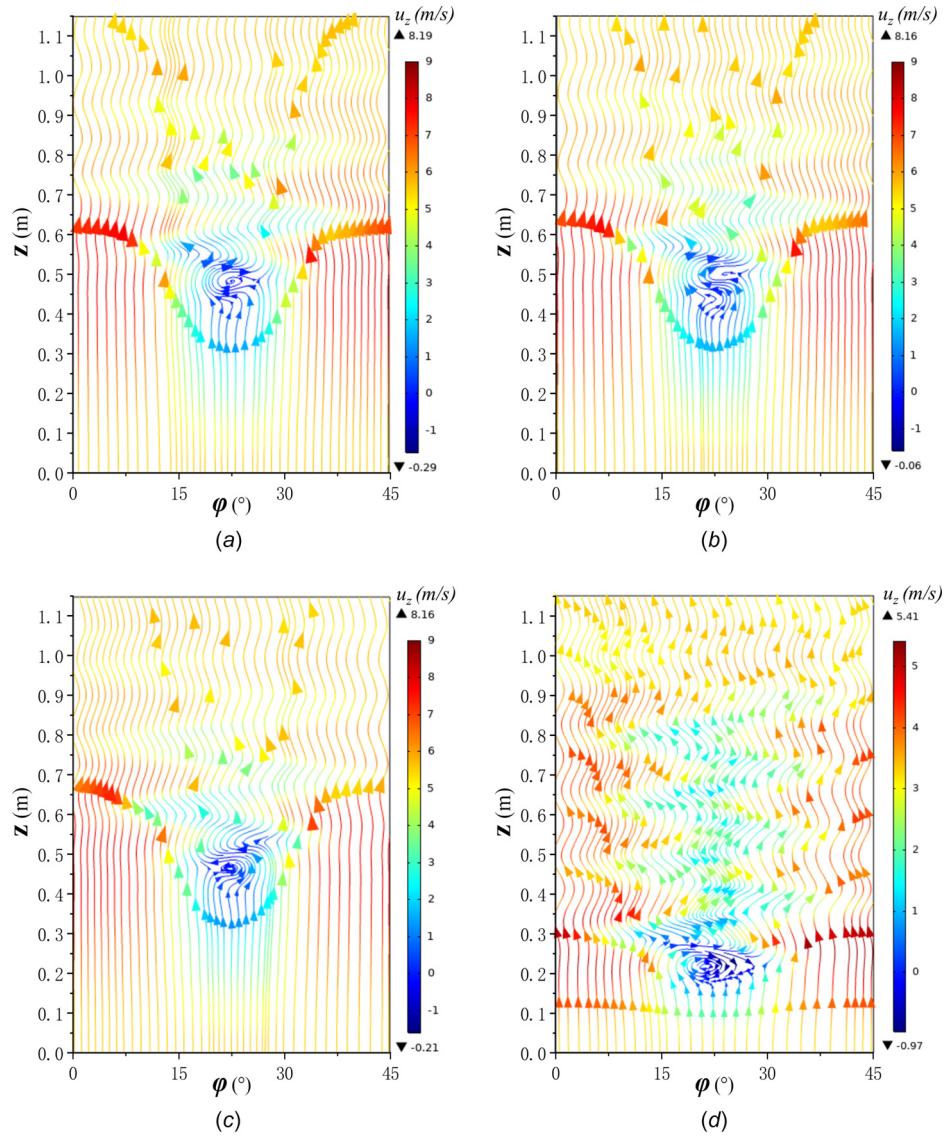

Fig. 8 Flow streamlines in the φ–z plane ($r = 0.148$ m) at ((*a*)–(*c*)) 3.4 m^3/min and (*d*) 2.0 m^3/min. (*a*) Q = 3.4 m^3/min, the first half period, (*b*) Q = 3.4 m^3/min, the transitional, (*c*) Q = 3.4 m^3/s, the second half period, and (*d*) Q = 2.0 m^3/s

forms. Initially, the vortex rotates anticlockwise and its strength increases. Then it weakens in both strength and scale and another smaller vortex with clockwise rotation appears. After that, the former vortex disappears and the later one grows in both strength and scale. This evolution is repeated with the external traveling magnetic field. Due to the alternative pair of vortices in the channel, the flow field downstream has been significantly influenced and the flow streamline behaves wave-like.

The flow structure at 2.0 m^3/min (Fig. 8(*d*)) is evolved similarly to the processes at 3.4 m^3/min while the location of the rotating vortex or vortical dipole shifts toward the inlet ($z = 0.18$ m) indicating the earlier occurrence of unstable flow. It should be noticed that due to the limitation in the modeling circumferential length of the model, the vortex occurring at the low flow rates could grow larger. The vortical size has been confined in the 1/8 section of the pump channel. However, the confinement on the vortex size will not hinder the investigation on the mechanism for the inception of unstable flows.

3.2.2 Azimuthal Profile of Axial Velocity at Different Axial Positions. The axial velocity profiles along the azimuthal direction are depicted in Figs. 9(*a*)–9(*d*) at four flow rates. The transient axial velocity is time-averaged through the last 20 current cycles and normalized by the average velocity (flow rate divided by the area of φ–r cross section) and at different axial positions in each figure. Here, $z = -0.1$ m and $z = 0.95$ m are located at the upstream and downstream of the electromagnetic section ($0 < z < 0.85$ m).

It is clearly illustrated that the flow deviates from a uniform distribution in the electromagnetic section regardless of the flow rate. Consisting with the observations in Figs. 7 and 8, the axial velocity in the middle sector gradually decelerates along the flowing direction while that in the two lateral sectors gradually accelerates in order to maintain the mass conservation. This tendency is retained until the vortex flow appears in the channel. However, the flow pattern can retain stable and symmetrical with the decreasing flow rate until the axial velocity in the middle section reduces to nearly zero at 4.0 m^3/min, at which the initially small vortex appears near the exit of the electromagnetic section (shown in Fig. 7(*d*)). This fact is also observed in other Refs. [2,10], and [11]. Further reducing the flow rate, the axial velocity profile becomes more nonuniform and the axial velocity in the middle sector can be negative, indicating a permanent vortex occurring in the pump channel. The region with the lowest axial velocity in the curve corresponds to the site of the occurring vortex. Moreover,

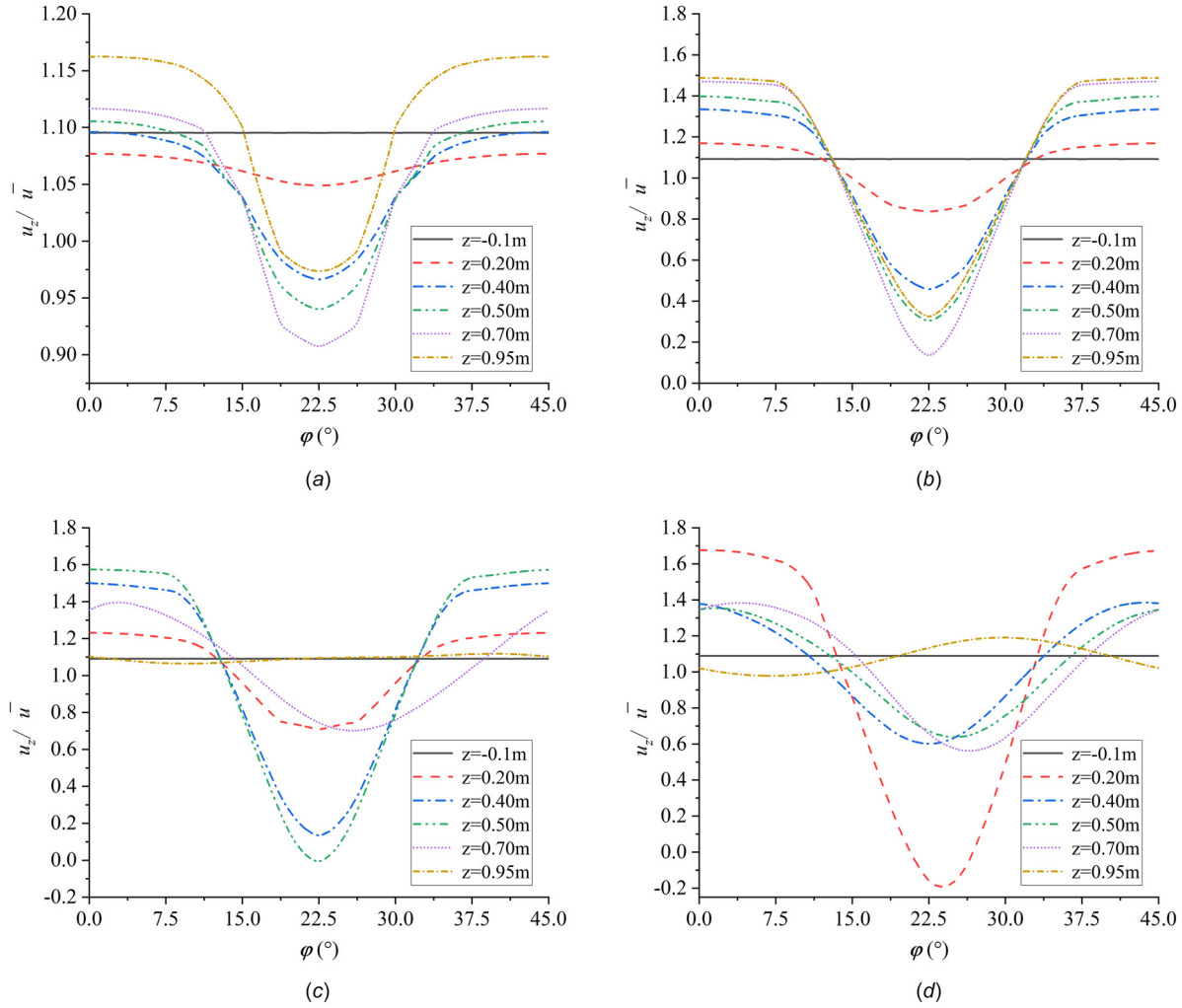

Fig. 9 Azimuthal profile of axial velocity at various flow rates and axial positions: (*a*) $Q = 7.0\ m^3/min$, (*b*) $Q = 4.0\ m^3/min$, (*c*) $Q = 3.4\ m^3/min$, and (*d*) $Q = 2.0\ m^3/min$

the velocity profiles become asymmetrical in the azimuthal direction at $2.0\ m^3/min$, which is related to the vortex and the wave-like flow presented downstream in the channel. The reason for the observed phenomena will be explained in Sec. 4.

3.2.3 Flow Structures Viewed From the Meridian Plane. The flow in different meridian planes along the azimuthal direction is not identical due to the unstable flow presented in the azimuthal plane. Two typical meridian planes were created at $\varphi = 7.5$ deg and 22.5 deg, respectively, as shown in Fig. 1(*c*). The former is located in the middle of the sector with $\varphi = 0$–15 deg while the latter is located in the middle of the pump channel. Since the flow can maintain stable velocity field when the flow rate is above 60% of the nominal rate as seen in the azimuthal plane, the flows in the meridian planes show the typical behavior of the Hartmann flow in channel where a flat velocity profile is located in the bulk of channel and decays rapidly to zero in the near-wall regions. The flow structures at those flow rates are not presented in this work for limiting the paper length.

Figures 10(*a*) and 10(*b*) show the velocity vectors at different times in the two meridian planes at $3.4\ m^3/min$. It can be seen that there is no reverse flow or vortex in the $\varphi = 7.5$ deg plane and the axial velocity is always positive and behaves like the Hartmann flow in the channel. In the $\varphi = 22.5$ deg meridian plane, more complex flow structures are observed. The velocity profile in the radial direction is nonuniform even in the very beginning time and the velocity near the outer duct is always smaller than that at the inner side. At $t = 0.082$ s, the flow at $z = 0.4$–0.45 m is reversed and separated initially from the outer side and then, the reversed flow region extends to both the downstream and the inner side. At $t = 0.15$ s, the flow is completely reversed after $z = 0.45$ m, indicating the establishment of the unstable region as seen in Fig. 10(*b*). At $t = 0.6$ s, in the region after $z = 0.70$ m, the reverse flow disappears and the fluid velocity changes to a positive value. The phenomena demonstrate clearly that the flow pattern in the meridian plane is closely correlated to the flow structure in the azimuthal plane. The initial occurrence of reversed or vortex flows happens in the azimuthal plane near the outer duct.

4 Discussion

4.1 Governing Mechanisms of Fluid Kinetic Energy. From studying the velocity evolution in time, it is found that the unstable flows, such as reversed and vortex flows, are originated from the loss of uniformity of the velocity profile in the azimuthal direction. In order to find the reason for the loss, it is useful to transform the fluid Navier–Stokes equation in the form of fluid kinetic energy K, which is expressed as

$$\frac{dK}{dt} = \int \boldsymbol{u}\frac{\partial \boldsymbol{u}}{\partial t}dV = -\int \nabla\cdot\left(\boldsymbol{u}\frac{p}{\rho}\right)dV - \int \nabla\cdot\left(\frac{1}{2}|\boldsymbol{u}|^2\boldsymbol{u}\right)dV - \nu\int \nabla\cdot(\boldsymbol{\omega}\times\boldsymbol{u})dV - \nu\int \boldsymbol{\omega}^2 dV + \int \boldsymbol{u}\cdot\frac{\boldsymbol{F}}{\rho}dV \quad (5)$$

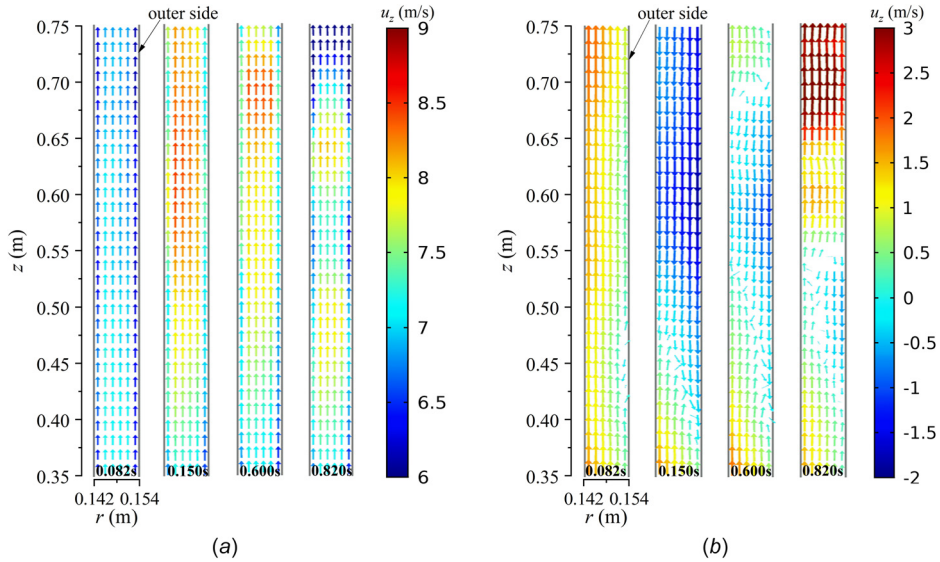

Fig. 10 Velocity vectors in different *r–z* planes under $Q = 3.4$ m^3/min: (*a*) $\varphi = 7.5$ deg and (*b*) $\varphi = 22.5$ deg

The second term at the right side can be ignored due to its relatively marginal value compared with other terms. Therefore, the other four terms (mechanisms) control the change of fluid kinetic energy in the pump channel. If the net value at the right side is positive, the local flow velocity will be continuously accelerated. Therefore, drawing the contours of the terms can provide an insight in how the fluid kinetic energy changes, as well as the fluid velocity.

Although the time derivative of K is transient, we first present time-averaged values of the four terms through the 11–20th simulated cycles (0.2–0.4 s) as shown in Figs. 11(*a*)–11(*d*). In order to show the electromagnetic region of the pump channel, the inlet and outlet of this region are, respectively, referred as to the front end and back end as seen in Fig. 11(*a*). The reason for this period is because the vortices underwent the inception and initial growing during this time. The studied case is $Q = 3.4$ m^3/min and the monitoring φ–z plane is $r = 0.148$ m. This figure clearly illustrates that the pressure and Lorentz force terms dominate the time evolution of fluid kinetic energy since their magnitudes are much larger than the other two terms related to fluid vorticity.

As for the pressure term shown in Fig. 11(*a*), negative value is presented in two lateral sectors of the pump channel while positive value is shown in the middle sector. The distribution indicates that the pressure field developed in the pump channel decelerates the flow at the two lateral sectors and accelerates the flow in middle. On the contrary, the Lorentz force term shows the opposite effect, as shown in Fig. 11(*d*). It is well explained that two factors compete with each other to finally determine the change of fluid kinetic energy and the fluid velocity. In addition, the third term which is known as vortex force shown in Fig. 11(*b*), can also provide a minor contribution. It can be seen that the positive value of vortex force term is presented in the interfacing area between the middle sector and two lateral ones, where the strong vortical structures are found. In the area of the electromagnetic section outlet, the vortex force will dissipate the fluid kinetic energy from the two lateral sectors to the middle one. In other words, the velocity profile tends to be uniform. As shown in Fig. 11(*c*), the fourth term is related to the flow enstrophy, which is the essential of kinetic energy dissipation no matter of the boundary conditions. It is not unusual that very small values prevail in the major area and the flow has limited energy dissipation in the region without the unstable flows. However, significant negative value is found in the two interfacing areas because of strong shear stress created by the vortex and the surrounding flow. It should be noted that the viscosity in Eq. (5) has already considered the combined effect of both molecular viscosity and turbulence.

In a sum, the net time-averaged value in the monitor φ–z plane is illustrated in Fig. 11(*e*). The flow in the middle sector is decelerated from $z = 0$ m to $z = 0.25$ m, where dK/dt is negative. Meanwhile, the flow in the two lateral sectors is accelerated from $z = 0.1$ m to $z = 0.65$ m. At the outlet of the pump's electromagnetic section, the flow is accelerated first and decelerated once it leaves the electromagnetic section. This figure clearly shows that the flow velocity is generally reduced in the middle sector while it is increased at two lateral sides due to the combined effect of the four mechanisms.

Figures 12(*a*)–12(*d*) show the azimuthal profiles of the time-averaged values of different terms in Eq. (5) at specified axial positions in the monitoring φ–z plane at $Q = 3.4$ m^3/min. The typical three axial positions were chosen to correspond to the stable flow region ($z = 0.2$ m), the inception of unstable flow ($z = 0.4$ m) and the region after the unstable flow ($z = 0.7$ m), respectively. As described above, the pressure and Lorentz force terms are competing and the other terms give minor effects. At the entrance of the electromagnetic section, $z = 0.2$ m, the positive Lorentz force term is stronger than the negative pressure gradient term at the two lateral sectors; thus, the dK/dt is positive and the flow is accelerated. However, the flow is decelerated in the middle sector because of the negative dK/dt. When the flow moves at the inception location of unstable flow, $z = 0.4$ m, the two competing mechanisms nearly cancel out in the middle sector ($dK/dt \approx 0$), indicating the flow stops deceleration. In fact, the flow losses completely positive velocity at this position and becomes reversed and swirling flows.

When the position is moving to $z = 0.7$ m, the contributions of pressure gradient and Lorentz force terms tend to be equal and the net effect is approximately close to zero, indicating a new balance established between the two forces. In the middle part, the signs of the two terms are changed oppositely, because a constant reversed flow is established in this area as shown in Fig. 10(*b*). When flow leaves the electromagnetic section, such as at $z = 1.0$ m, the contribution of Lorentz force is vanished and the associated pressure term becomes very limited. At this position, dK/dt is dominantly negative through the azimuthal direction and it is determined by the vortex force term. That is to, say, the wave-like flow takes over the role in dissipating the fluid kinetic energy and reducing the flow velocity.

4.2 Lorentz Force Versus Pressure Gradient. Based on the above-mentioned content, the inception of unstable flows is

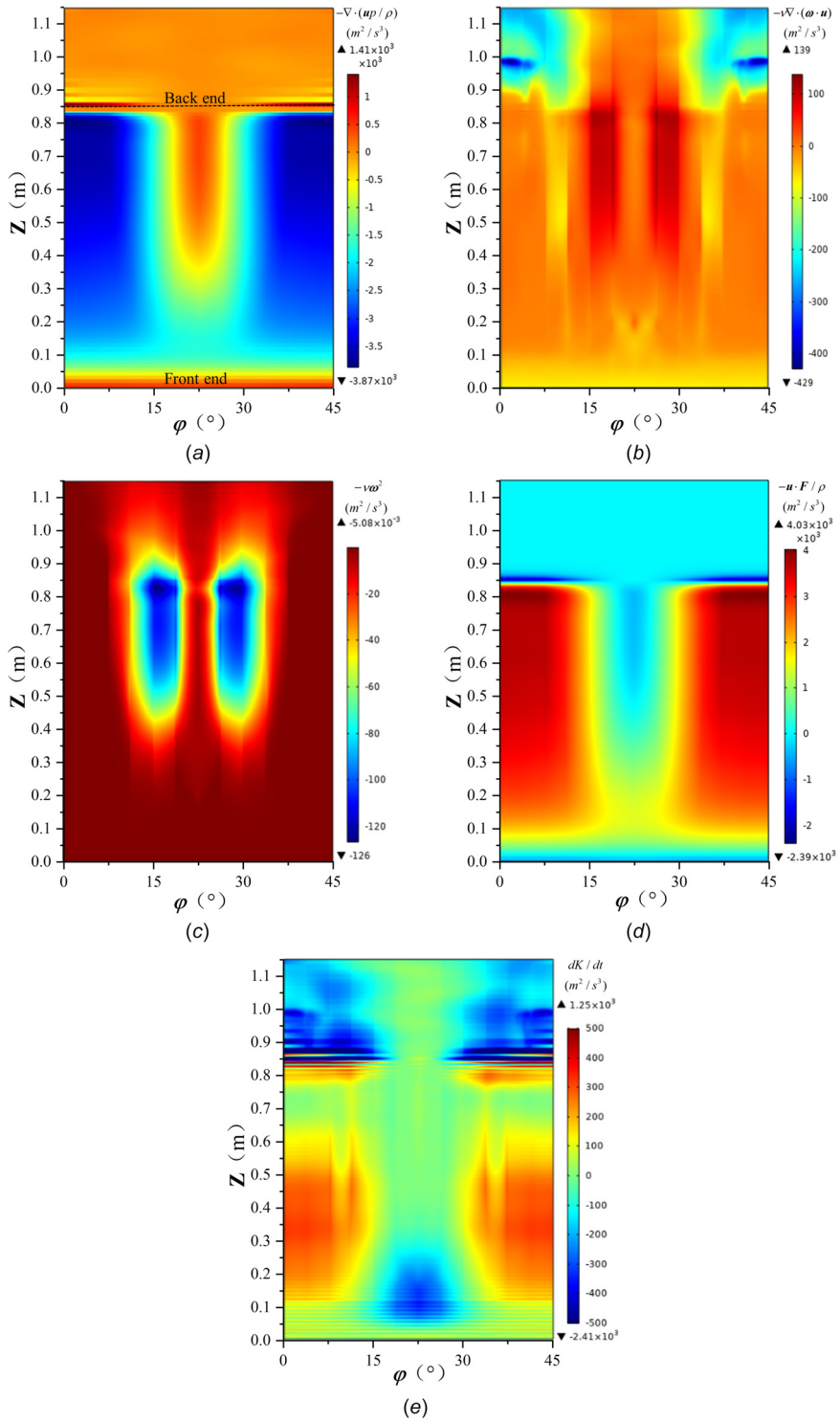

Fig. 11 Contours of time-averaged values of different terms in Eq. (5) at $Q = 3.4$ m^3/min: (*a*) pressure term, (*b*) vortex force term, (*c*) enstrophy term, (*d*) Lorentz force term, and (*e*) *dK/dt*

ascribed to the flow deceleration in the middle sector and acceleration in two lateral sectors. The reason for the heterogeneous behavior lays in the competition between the contributions of pressure gradient and Lorentz force terms in the fluid kinetic energy equation. Let us look at the flow from the viewpoint of Navier–Stokes equation again. Figure 13 shows the time-averaged axial Lorentz force and pressure gradient (0.2–0.4 s) along the azimuthal direction at three axial positions. By eliminating the influence of velocity in the terms of Eq. (5), large difference is found between the axial Lorentz force and pressure gradient. Due to the presence of air gap between two outer stators, the induced magnetic field in the middle sector is smaller than those at two lateral sectors, resulting in a large discrepancy in the axial Lorentz force, as shown in Fig. 13(*a*). Nevertheless, one can see in Fig. 13(*b*) that the axial pressure gradient keeps relatively constant in the azimuthal direction with a comparative magnitude with the Lorentz force. It is known that the positive Lorentz force provides the energy into the flow and the energy is conserved as the increasing

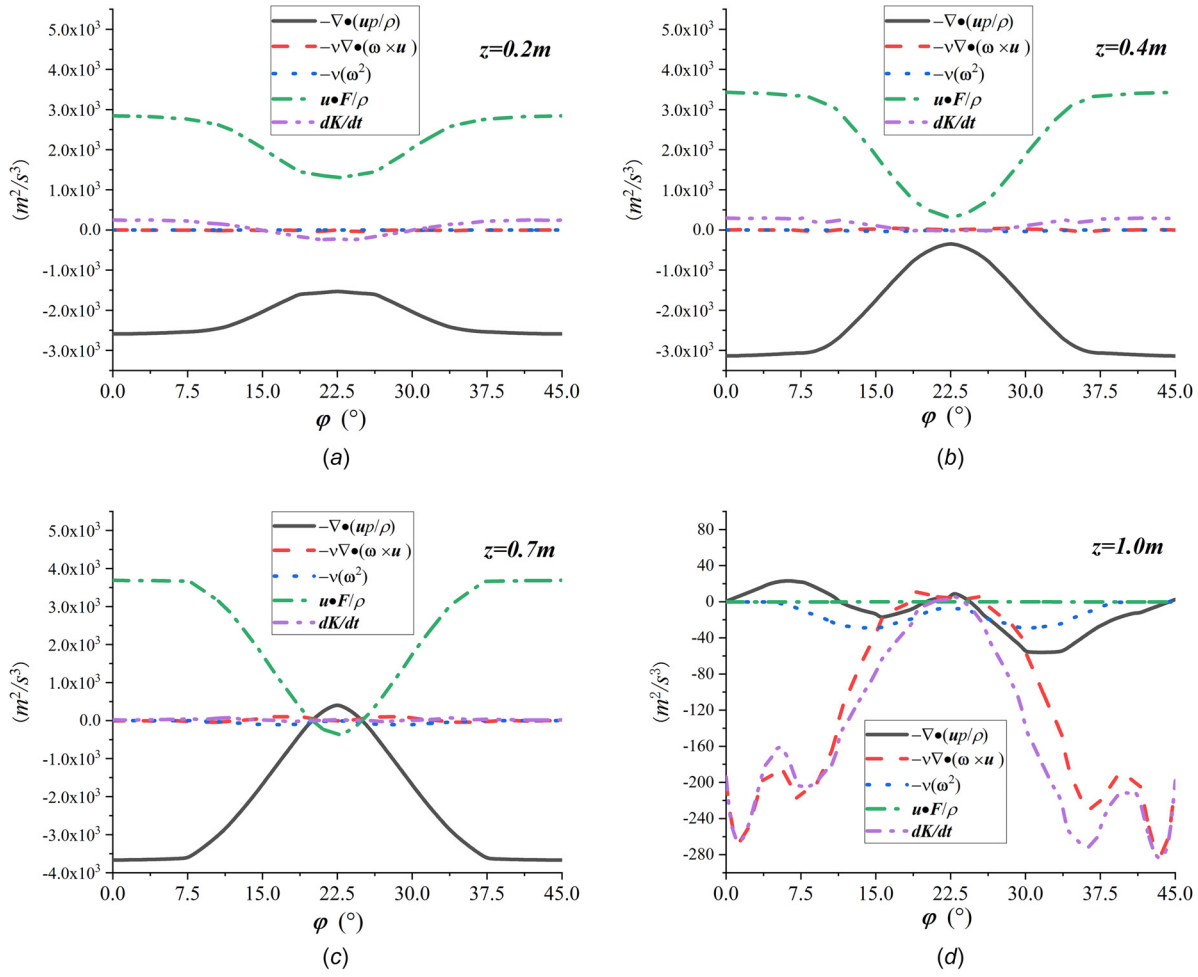

Fig. 12 Azimuthal profiles of time-averaged values of different terms in Eq. (5) at different axial positions and in the middle φ–z plane: (*a*) $z = 0.2$ m, (*b*) $z = 0.4$ m, (*c*) $z = 0.7$ m, and (*d*) $z = 1.0$ m

flow pressure, which results in a positive pressure gradient along the axial direction. However, the lower Lorentz force in the middle sector is insufficient to develop the local pressure gradient matching to that in the flow at two lateral sectors and therefore, the flow in the middle sector has to lose its kinetic energy (reducing the velocity) to compensate the deficit. It is noted that the pressure gradient is less sensitive to adapt to the discrepancy in the Lorentz force, forcing the flow in the middle sector losing its kinetic energy to compensate the deficit in pressure development. This mismatch exists throughout the electromagnetic section. If the flow velocity in the region of smaller Lorentz force reduces to zero and reverses, the vortex will appear due to strong shear stress in the flow.

This finding could be applied to explain the unstable flow at other flow rate conditions. The time-averaged axial Lorentz force and pressure gradient under different flow rates and at the axial position $z = 0.4$ m are presented in Fig. 14. The azimuthal profile of axial Lorentz force changes very little with the reducing flow rate except for a lower magnitude occurring at the nominal flow rate. It illustrates that the Lorentz force in the middle sector is always smaller than that at two lateral sectors. On the other hand, the axial pressure gradient always keeps constant in the azimuthal direction no matter of what the flow rate is, as shown in Fig. 14(*b*). Therefore, Lorentz force in the middle sector is insufficient to input energy into the flow for increasing the local pressure and the flow in this sector has to reduce its velocity or kinetic energy to increase the flow pressure. When the pumping flow rate is above 4.0 m^3/min, the flow remains stable even though its velocity in the middle sector reduces. Further reducing the flow rate, the flow in the middle section loses all axial velocity and create strong shear stresses with the flow at two lateral sectors, resulting in the inception of vortices in the channel.

4.3 Analytical Expression of Axial Lorentz Force. From the analysis in Sec. 4.2, we see that the axial Lorentz force profile has a great influence on the flow stability, so it is critical to understand how the axial Lorentz force is determined by other factors (e.g., fluid velocity and magnetic field). In this part, an analytical expression of the Lorentz force is derived. Although the MHD flow in the ALIP's pump channel can experience 3D movement, simplifying the flow in a 2D problem is a good approximation before the occurrence of reversed and vortex flows. The time-averaged axial Lorentz force is defined as follows:

$$\boldsymbol{F}_{lz} = -\frac{1}{2}\Re[\boldsymbol{B} \times \boldsymbol{J}^*] \tag{6}$$

where $\boldsymbol{B}$ is the magnetic flux density and $\boldsymbol{J}^*$ denotes the conjugate complex of the induced current density. In this work, we are interesting in the axial Lorentz force $F_{lz,z}$ before the flow losing stability. This force is expressed as

$$F_{lz,z} = -\frac{1}{2}\Re[B_r \cdot J_\varphi^*] \tag{7}$$

where B_r denotes the radial component of the magnetic flux density and J_φ^* is the conjugate complex of the azimuth component of the induced current. They are calculated as

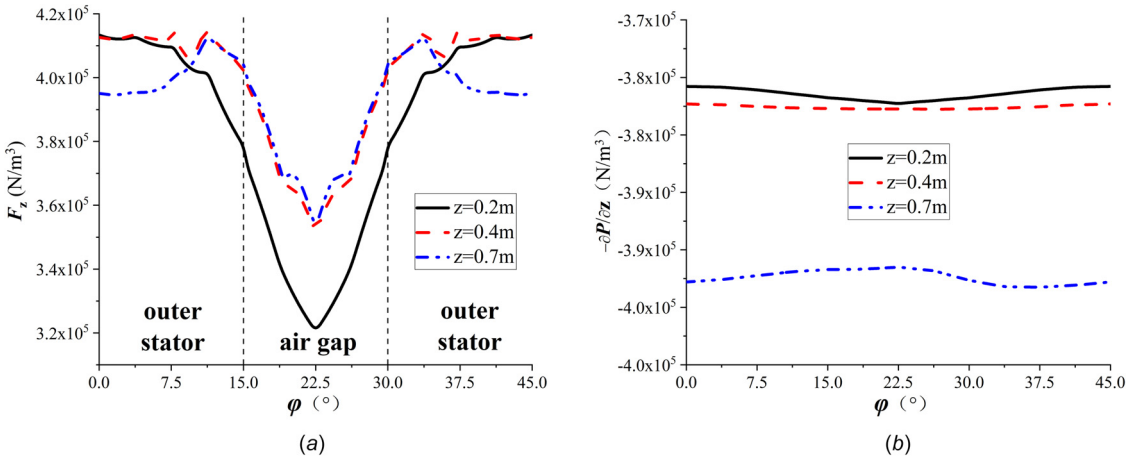

Fig. 13 Azimuthal profiles of time-average axial component of (*a*) Lorentz force and (*b*) pressure gradient at different axial positions under $Q = 3.4$ m^3/min

$$B_r = \frac{\partial A_z}{r\partial\varphi} - \frac{\partial A_\varphi}{\partial z} \tag{8}$$

$$J_\varphi = \sigma(-i\omega A_\varphi + u_z \cdot B_r) \tag{9}$$

where A_φ is the azimuthal component of magnetic vector $\boldsymbol{A}$, which satisfies $\boldsymbol{B} = \nabla \times \boldsymbol{A}$. σ is the electric conductivity, $\omega = 2\pi f$ and f, the input current frequency.

Base on the 2D approximation, $\boldsymbol{A}$ is axisymmetric in the cylindrical coordinate; thus, $(\partial A_z/\partial\varphi) = 0$ and $B_r = -(\partial A_\varphi/\partial z)$. Considering the cosinoidal input current and ignoring the end effect, the stimulated B_r and A_φ can be written in the following form:

$$B_r = \bar{B}_{r,\text{amp}} e^{i(\omega t - kz + \phi)}, \quad (k > 0) \tag{10}$$

where $\bar{B}_{r,\text{amp}}$ is the average amplitude of the radial component of induced magnetic flux density, k represents the wave number in the z direction (axial direction), and ϕ, the phase angle. Thus

$$A_\varphi = \bar{A}_{\varphi,\text{amp}} e^{i(\omega t - kz + \phi - \pi/2)} \tag{11}$$

where $\bar{A}_{\varphi,\text{amp}} = \frac{1}{k}\bar{B}_{r,\text{amp}}$.

By substituting Eqs. (10) and (11) into Eq. (9), the conjugate complex of the induced current density is expressed as

$$J^*_\varphi = \sigma\left(u_z - \frac{\omega}{k}\right)\bar{B}_{r,\text{amp}} e^{-i(\omega t - kz + \phi)} \tag{12}$$

By combining Eqs. (7), (10), and (12), the axial Lorentz force can be obtained as follows:

$$F_{lz,z} = -\frac{1}{2}\Re\left[B_r \cdot J^*_\varphi\right] = \frac{1}{2}\sigma\left(\frac{\omega}{k} - u_z\right)\bar{B}^2_{r,\text{amp}} \tag{13}$$

From Eq. (13), it can be seen that the magnitude of axial Lorentz force is determined by the input current angular frequency ω, the wave number k, the axial velocity u_z, and the square of the average amplitude of the radial component of induced magnetic flux density $\bar{B}_{r,\text{amp}}$. If the input frequency, the wave number, and the average magnetic flux density are constant (no disturbance in the magnetic field), the magnitude of the axial Lorentz force only depends on the axial velocity. That is to, say, the larger the axial velocity means the smaller axial Lorentz force.

This expression can be validated with the numerical results. In the studied pump, $\sigma = 7.3 \times 10^6$ S/m, $\omega = 314$ Hz, and $k = 22.4$. The average axial velocities are 10.45, 7.90, and 6.63 m/s at 7.0, 5.3, and 4.4 m^3/min and the average $\bar{B}_{r,\text{amp}}$ are 0.155, 0.141, and 0.128 T obtained from the numerical results. Putting the values into Eq. (13), the time-averaged axial Lorentz force $F_{lz,z}$ is 3.13×10^5, 4.37×10^5, and 4.41×10^5 N/m^3, which are consistent with the simulation results shown in Fig. 6.

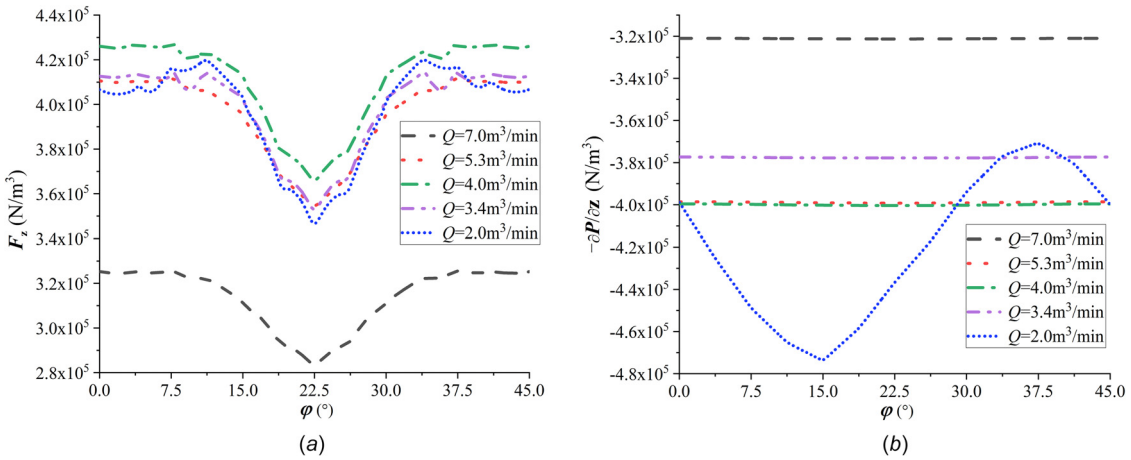

Fig. 14 Azimuthal profiles of time averaged axial component of (*a*) Lorentz force and (*b*) pressure gradient at $z = 0.4$ m under different flow rates

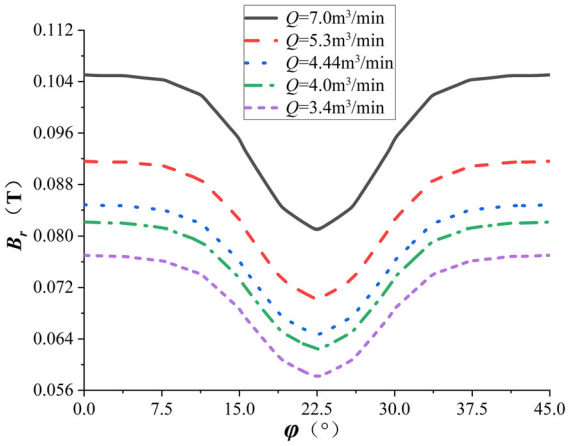

Fig. 15 Azimuthal profile of time-averaged B_r at different flow rates with uniform inlet velocity

4.4 Effects of Velocity and Magnetic Field on the Axial Lorentz Force Profile. Based on Eq. (13), the axial Lorentz force could become nonuniform if the distributions of u_z and B_r are nonuniform in either azimuthal or radial directions. Let us first consider a disturbance existing in the azimuthal direction of B_r. The disturbance is normally introduced by the configuration of stators (discretized stators or deviation from concentricity between stator and channel). Given for a uniform velocity profile, the axial Lorentz force is proportional to the square of B_r. Its profile will be coincident with the B_r profile. Figure 15 shows the azimuthal profiles of B_r in the middle position of the pump channel at different flow rates with uniform inlet velocity in this work. It is seen that the magnitude of B_r is slightly decreased with the reducing flow rate, indicating the influence of average velocity on B_r. The B_r profiles, however, keep similar at different flow rates. B_r is smaller in the middle sector than that in the two lateral sectors because of the presence of air gap between the two half outer stators. Even a small lower in B_r can create a square attenuation in the axial Lorentz force in the middle sector, which explains the large discrepancy in the axial Lorentz force shown in Figs. 13(*a*) and 14(*a*). When the flow goes into the electromagnetic section, the middle sector is continuously decelerated due to lower Lorentz force until its loss in velocity can balance the deficit between Lorentz force and pressure gradient. If the azimuthal nonuniformity of the magnetic field is sufficiently large and/or the average velocity is small enough, the positive velocity in the middle sector could be exhausted and unstable flow will occur in the flow channel, which has been verified in Sec. 3.

The second possible scheme lays in the axial velocity distribution. It can be simply created by imposing an azimuthal disturbance in the inlet velocity, expressed as Eq. (14). Here, α represents the azimuthal nonuniformity of the axial velocity, k_φ represents the wave number of the cosine curve and φ_0, the initial phase. k_φ is defined as $k_\varphi = 2\pi/\lambda_\varphi$ and $\lambda_\varphi = 2\pi/N$, where N denotes the number of disturbing cycles throughout the channel perimeter

$$u_{z,\text{inlet}} = \bar{u}_z[1 + \alpha\cos(k_\varphi\varphi + \varphi_0)] \tag{14}$$

Figure 16(*a*) illustrates the azimuthal profiles of axial velocity with different values of α, k_φ, and φ_0 at $Q = 3.4$ m^3/min and $0 < \varphi < \pi/4$. The time-averaged axial Lorentz force on the fluid calculated by Eq. (13) is shown in Fig. 16(*b*) with $\bar{B}_{r,\text{amp}} = 0.105$ T at the average velocity of 5 m/s. It is found that the high velocity region always corresponds to the low axial Lorentz force. It can also be verified from Eq. (13) that the axial Lorentz force is proportional to the relative velocity between the traveling wave and fluid. Recalling the analysis in Sec. 4.2, the flow lost the velocity in the region where the induced Lorentz force cannot compete with the developed pressure gradient. In this case, the high velocity region will decrease the velocity because of the lower Lorentz force. Therefore, the nonuniformity of the inlet velocity will be gradually flattened. If the electromagnetic section is long enough, the velocity profile tends to be even in the azimuthal direction and the unstable flow will not occur in the channel.

However, things will become complicated when the fluid velocity can influence the magnetic flux density in the channel. The axial Lorentz force profile will be determined by both the velocity and magnetic flux density while the magnetic flux density is implicitly influenced by the velocity. It is useful to analyze the interaction between the conducing fluid velocity and induced magnetic flux density in the formulation of magnetic induction equation, which is written as

$$\frac{\partial \boldsymbol{B}}{\partial t} = \frac{1}{\mu\sigma}\nabla^2\boldsymbol{B} + \nabla\times(\boldsymbol{u}\times\boldsymbol{B}) \tag{15}$$

Still, we are interesting in the radial component of the induced magnetic flux density B_r. The equation is reduced as

$$\begin{aligned}&\frac{\partial B_r}{\partial t} + \left\{\left(u_r\frac{\partial B_r}{\partial r} + \frac{u_\varphi}{r}\left(\frac{\partial B_r}{\partial \varphi} - B_\varphi\right) + u_z\frac{\partial B_r}{\partial z}\right)\right.\\ &\left.-\left(B_r\frac{\partial u_r}{\partial r} + \frac{B_\varphi}{r}\left(\frac{\partial u_r}{\partial \varphi} - u_\varphi\right) + B_z\frac{\partial u_r}{\partial z}\right)\right\}\\ &= \frac{1}{\mu\sigma}\left(\left(\frac{\partial^2 B_r}{\partial r^2} + \frac{\partial B_r}{r\partial r}\right) + \frac{1}{r^2}\left(\frac{\partial^2 B_r}{\partial \varphi^2} - 2\frac{\partial B_\varphi}{\partial \varphi} - B_r\right) + \frac{\partial^2 B_r}{\partial z^2}\right)\end{aligned} \tag{16}$$

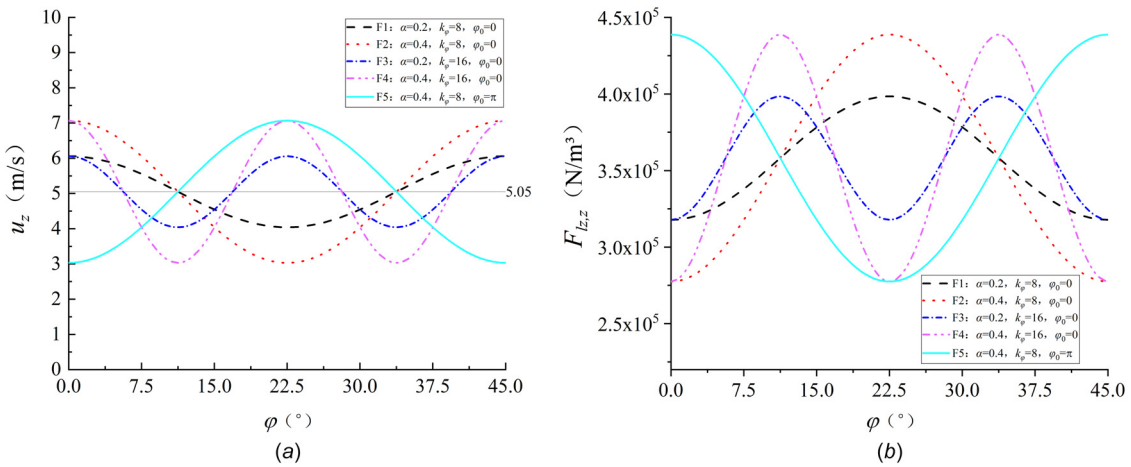

Fig. 16 Azimuthal profiles of (*a*) the inlet velocity and (*b*) axial Lorentz force with different α, k, and φ_0

Here, $u_r = u_\varphi = 0$ as it is assumed the flow still remains steady in the channel. Before the unstable flow occurs, the azimuthal component of the induced magnetic flux density B_φ is so small that it can be ignored. Then, the equation is transformed in the nondimensional form using a length scale $l_0 = d$ (the channel height), a velocity scale $u_0 = c$ (the traveling wave velocity $c = \omega/k$), a time scale $T_0 = d/c$, and the scale of the magnetic flux density $B_0 = c(\mu\rho)^{1/2}$ as

$$\frac{\partial B_r^*}{\partial t^*} + u_z^* \frac{\partial B_r^*}{\partial z^*} = \frac{1}{\mathrm{Rm}} \left(\left(\frac{\partial^2 B_r^*}{\partial r^{*2}} + \frac{\partial B_r^*}{r^* \partial r^*} \right) + \frac{1}{r^{*2}} \left(\frac{\partial^2 B_r^*}{\partial \varphi^2} - B_r^* \right) + \frac{\partial^2 B_r^*}{\partial z^{*2}} \right) \tag{17}$$

where the magnetic Reynolds number is defined as $\mathrm{Rm} = \mu\sigma dc$. The change in B_r with time is determined by the convection by the fluid axial velocity and the dissipation by its spatial derivatives. Based on Eq. (13), $F_{lz,z}$ could become nonuniform if an azimuthal disturbance in axial velocity can evoke the disturbance in B_r. Given there is a disturbance in the inlet velocity, it can be approximately defined as Eq. (14). Then, the induced B_r can be approximated in the form of

$$B_r = \bar{B}_r[1 + \beta\cos(k_r r + r_0)][1 + \gamma\cos(k_\varphi \varphi + \varphi_0)]\cos(\omega t - kz + \phi) \tag{18}$$

where $\bar{B}_r$ denotes the average value of the magnetic flux density. The disturbance in B_r due to the velocity is represented in the same form as the nonuniform axial velocity but with a different coefficient γ to represent the magnetic nonuniformity. In order to compare the magnetic disturbance in the radial direction, another cosinoidal form is defined in the radial direction and k_r represents the wave number along this direction. Substituting the nondimensional forms of Eqs. (14) and (18) into Eq. (17) and the magnetic induction equation for B_r^* becomes as

$$\begin{aligned} &(-\omega^* + k^* \bar{u}_z^* W)\sin(\omega^* t^* - k^* z^* + \phi^*) \\ &= -\frac{2\pi}{\mathrm{Rm}} \left(\left[k_r^{*2}(1 - 1/L) + \frac{k_r^*}{r_{\mathrm{mid}}^*} \frac{\beta \sin(k_r^* r^* + r_0^*)}{2\pi L} \right] + \frac{1}{r_{\mathrm{mid}}^{*2}} \left[k_\varphi^{*2}(1 - 1/M) + \frac{1}{4\pi^2} \right] + k^{*2} \right) \cos(\omega^* t^* - k^* z^* + \phi^*) \\ &W = 1 + \alpha\cos\left(k_\varphi^* \varphi + \varphi_0\right), L = 1 + \beta\cos(k_r^* r^* + r_0^*), M = 1 + \gamma\cos\left(k_\varphi^* \varphi + \varphi_0\right) \end{aligned} \tag{19}$$

Here, the angular frequency ω is normalized by $2\pi/T_0$, the wave numbers k_r and k are normalized by $2\pi/d$. k_φ is originally a dimensionless number and it is defined as $k_\varphi^* = k_\varphi/(2\pi)$ in order to have the same form as k_r^* and k^*. Since the height of the channel d is much smaller than the radius of the ALIP channel, the radius of the central cylinder of the channel r_{mid} is used to instead of r in Eq. (17).

The definitions of different terms in Eq. (19) are listed in Table 3. It is seen that the time derivative and convective terms possess the same phase but opposite sign. The magnitude of the time derivative is proportional to the angular frequency, which is equal to the input current frequency. The magnitude of the convective term is proportional to the product of the nondimensional axial wave number and axial velocity. The dissipation term at the right side is consisted of three components, each being mainly proportional to the square of its wave number (the second terms in $C_{d,r}$ and $C_{d,\varphi}$ are usually much smaller than the first ones). Meanwhile, it is inversely proportional to the magnetic Reynolds number. Particular interest is paid on the azimuthal dissipation term, which is also inversely proportional to the square of the mean channel radius, indicating that the azimuthal nonuniformity will occur more easily in larger ALIPs. The dissipating effects of B_r in the radial and azimuthal directions are adaptable through the nonuniformity β and γ. Hereby, the relative role of different mechanisms for B_r evolution can be estimated based on analyzing the magnitude of each term.

The parameters from the studied pump (summarized in Table 4) are input into the corresponding terms in Eq. (19). Special attention is paid on the value of k_φ^*. As the model in this work contains only 1/8 of the perimeter of pump channel with the periodical condition, k_φ^* should be equal to $4/\pi$ if a completely disturbing cycle is defined along the azimuthal length while it should be set as $1/(2\pi)$ if one disturbing cycle is defined along the whole perimeter. Since the radial variation of B_r is normally smaller than its counterparts in the other two directions, it is assumed $\lambda_r = 8d$ for a conservative approximation and the radial wave number $k_r = 2\pi/\lambda_r = 2\pi/(8d)$. Thus, $k_r^* = 1/8$ since $k_r^* = k_r/(2\pi/d)$. In the magnitude calculation, all trigonometric functions are set as 1. $\alpha = \beta = \gamma = 0.5$ is assumed to estimate the strengths of different

Table 3 Definitions of different terms in Eq. (19)

Equation terms	Definitions
The time derivative term (Ct)	$-\omega^* \sin(\omega^* t^* - k^* z^* + \varphi^*)$
The convective term (C_v)	$k^* u_2^{-*} W \sin\ (\omega^* t^* - k^* z^* + \varphi^*)$
The radial dissipation term (Cd,r)	$-\frac{2\pi}{\mathrm{Rm}} \left(k_r^{*2}(1 - 1/L) + \frac{k_r^*}{r_{\mathrm{mid}}^*} \frac{\beta \sin(k_r^* r^* + r_0^*)}{2\pi L} \right) \cos(\omega^* t^* - k^* z^* + \phi^*)$
The azimuthal dissipation term (Cd,φ)	$-\frac{2\pi}{\mathrm{Rm} \cdot r_{\mathrm{mid}}^{*2}} \left(k_\varphi^{*2}(1 - 1/M) + \frac{1}{4\pi^2} \right) \cos(\omega^* t^* - k^* z^* + \phi^*)$
The axial dissipation term (Cd,z)	$-\frac{2\pi}{\mathrm{Rm}} k^{*2} \cos(\omega^* t^* - k^* z^* + \phi^*)$

disturbances in a considerable variation. The magnitudes of five terms are presented in Table 4. It should be noted that the algebraic calculation among these coefficients makes no sense, since all values denote the scales of different terms and the time evolution of the variables is not accounted.

The time derivative term C_t is −0.043 while the convective term C_v with $u_z = 5.05$ m/s ($Q = 3.4$ m^3/min) is 0.023. Meanwhile, the axial dissipation term $C_{d,z}$ is −0.007 and the values of $C_{d,\varphi}$ and $C_{d,r}$ are −0.015 and −0.022. The larger the dissipation coefficient is, the smaller the nonuniformity of B_r is. The results show the radial dissipating effect is strongest and therefore, the radial profile of B_r is hardest to be disturbed. However, given that the azimuthally disturbing cycle covers the whole channel perimeter, i.e., $k_\varphi = 1$, $C_{d,\varphi}$ is reduced to −0.00085, indicating a significant loss of dissipating effect. The azimuthal variation of B_r will be increased much, resulting in a larger nonuniformity in the axial Lorentz force. Reminding the previous statement on the limitation of 1/8 sectional model, the unstable flows will occur more easily if the model was extended into a whole cylinder.

In another Ref. [3], the disturbance in the inlet velocity can significantly change the azimuthal distribution of the induced magnetic flux density. Therefore, the parameters of that pump are also listed in Table 4 and used to calculate the coefficients of Eq. (19). The values of C_t, C_v, and $C_{d,z}$ are −0.128, 0.08, and −0.016 while $C_{d,\varphi}$ and $C_{d,r}$ are −0.00067 and −0.006. It is seen that the time derivative and convection still play the dominant roles in determining B_r. The strengths of different terms can be compared between the two pumps as the nondimensional form is used. In that pump, the strengths of time derivative and convection are approximately three times larger while the axial dissipating effect is double. The imbalance between time derivative and convection is larger and need to be dissipated from two other directions. Nonetheless, the coefficients of azimuthal and radial dissipation are much smaller than their counterparts in the pump studied in this work, especially for $C_{d,\varphi}$. This can be attributed to the factors that the disturbing cycle in that pump was defined through the channel perimeter and the pump height d is significantly enlarged. Therefore, the azimuthal disturbance in the fluid velocity significantly change the azimuthal distribution of the magnetic field in that work since the azimuthal dissipating effect is extremely low and very sensitive to the variation of convective term.

Based on Eq. (19), the optimization schemes for increasing the flow stability in ALIP can be well understand. The unstable flow could be controlled by circumferentially installing several baffle plates along the channel length [7]. Therefore, the disturbance will be constrained in each independent subchannel and the wave number k_φ increases as the wavelength is shortened by the blockage of plates. The increasing wave number enhances the azimuthal dissipating effect and reduces the nonuniformity of B_r. Then, the nonuniformity in the Lorentz force is reduced significantly due to the term of $\bar{B}^2_{r,\text{amp}}$ in Eq. (13). Another optimization laid in the change of phase order [11], which equivalently decreases the wavelength of the traveling magnetic field. k_z is then increased, accompanied by the axial dissipating effect. This enhancement will delay the occurrence of nonuniform magnetic field in either azimuthal or radial direction.

Table 4 Parameters of the studied pumps in this work and Ref. [3]

Parameters (unit)	In this work	In Ref. [3]
ω (Hz)	314	125.6
λ (m)	0.28	0.6
c (m/s)	14	12
$\bar{u}_z$ (m/s)	5.05	5.05
d (m)	0.012	0.077
r_{mid} (m)	0.148	0.54
Rm	1.60	6.42
C_t	−0.043	−0.128
C_v	0.023	0.08
$C_{d,r}$	−0.022	−0.006
$C_{d,\varphi}$	−0.01465	−0.00067
$C_{d,z}$	−0.007	−0.016

5 Conclusions

In this work, a 3D numerical model was built to model a 1/8 ALIP with simplified geometry. The pump performance was successfully simulated and agreed well with the experimental results. The common flow characteristics in ALIP were well reproduced, such as DSF at both ends and Hartmann flow profile in the pump channel. The flow structures viewed in both the azimuthal and meridian planes were analyzed at different flow rates. The MHD flow in the pump channel behaved heterogeneous in the azimuthal direction. The flow in the middle sector was decelerated while it was accelerated in two lateral sectors. Reversed flow initially occurred near the outlet of the electromagnetic section, followed by the occurrence of vortices. The vortex was mainly located in the middle sector and its scale, strength, and rotating direction were varied with time. The position of the vortex inception moved upstream with the reducing flow rate. A wave-like swing was presented in the flow field after the vortex, introducing large disturbances in the flow velocity and pressure. From the meridian viewpoint, reversed flow initially occurred in the region near the outer duct and developed toward the inner side and downstream. It has shown that the initial unstable flow occurred in the azimuthal plane and near the outer duct.

The underlying mechanism for the nonuniform velocity field was disclosed by analyzing the governing equation of fluid kinetic energy. The discrepancy was found between the contributions of axial Lorentz force and pressure gradient. Further peeping the two parameters, the nonuniform axial Lorentz force and the relatively even pressure gradient in the azimuthal direction caused the nonuniform axial fluid velocity. If the loss in the velocity was not sufficient to compensate the deficit in Lorentz force, reversed flow happened and then vortex occurred. Finally, an analytical expression of the axial Lorentz force was developed and it demonstrates the axial Lorentz force is determined by the axial velocity and square of the radial magnetic flux density. The complex situation, in which the velocity variation could cause significant change in the magnetic field profile, was studied based on the dimensionless magnetic induction equation. The influence of disturbance in the axial velocity profile on the radial magnetic flux density and the resulting axial Lorentz force was estimated and discussed for two different real pumps. It was found that the dissipation of magnetic field in the pump channel is determined by both the magnetic Reynolds number and the wave number of disturbance in the magnetic field. The wave number could be varied significantly depending on the pump dimension and the wavelength of disturbing cycle. Finally, the mechanisms of several schemes for optimizing the flow stability in ALIP were explained based on the model.

Funding Data

- National Key R&D Program of China (Grant No. 2017YFC0404203).
- National Natural Science Foundation of China (Grant No. 51509110; Funder ID: 10.13039/501100001809).
- Key R&D Program of Jiangsu Province (Grant No. BE2016163).
- Senior Talent Fund of Jiangsu University (Grant No. 5501440001).

Nomenclature

A = magnetic vector
B = induced magnetic flux density

$\bar{B}_{r,\mathrm{amp}}$ = average amplitude of the radial component of induced magnetic flux density
c = synchronous velocity
$C_{d,r}$ = radial dissipation term
$C_{d,z}$ = axial dissipation term
$C_{d,\varphi}$ = azimuthal dissipation term
C_t = time derivative term
C_v = convective term
d = pump channel width
f = current frequency
F_{lz} = induced Lorentz force
F_z = axial volume force
J_e = external current density
J_0 = the equivalent current density magnitude
k = wave number along the axial direction
K = fluid kinetic energy
k_r = wave number along the radial direction
k_φ = wave number along the azimuthal direction
Rm = magnetic Reynolds number, $\mathrm{Rm} = \mu\sigma cd$
s = slip velocity, $s = 1 - \bar{u}/c$
$\bar{u}$ = average velocity
u_z = axial velocity
α = azimuthal nonuniformity of the axial velocity
β = radial nonuniformity of the magnetic flux density
γ = azimuthal nonuniformity of the magnetic flux density
Δp = pressure difference
Δp_{em} = electromagnetic pressure, $\Delta p_{\mathrm{em}} = \Delta p + \Delta p_h$
Δp_h = hydrodynamic pressure loss
μ = magnetic permeability of fluid
ν = total viscosity, $\nu = \nu_f + \nu_T$
ν_f = fluid viscosity
ν_T = turbulent viscosity
σ = electric conductivity of fluid
τ = pole pitch
ϕ = phase angle
ω = angular frequency, $\omega = 2\pi f$

References

[1] Yang, C. C., and Kraus, S., 1977, "A Large Electro-Magnetic Pump for High Temperature LMFBR Applications," Nucl. Eng. Des., **44**(3), pp. 383–395.
[2] Ota, H., Katsuki, K., Funato, M., Taguchi, J., Fanning, A. W., Doi, Y., Nibe, N., Ueta, M., and Inagaki, T., 2004, "Development of 160 m^3/Min Large Capacity Sodium-Immersed Self-Cooled Electromagnetic Pump," J. Nucl. Sci. Technol., **41**(4), pp. 511–523.
[3] Asada, T., Aizawa, R., Suzuki, T., Fujishima, Y., and Hoashi, E., 2015, "3D MHD Simulation of Pressure Drop and Fluctuation in Electromagnetic Pump Flow," Mech. Eng. J., **2**(5), p. 15–00230.
[4] Imazio, P. R., and Gissinger, C., 2016, "Instability in Electromagnetically Driven Flows—II," Phys. Fluids, **28**(3), p. 034102.
[5] Roman, C., 2013, "Studies of the Annular Linear Induction Pumps for Sodium Circuits Use in Nuclear Plants," International Youth Conference on Energy, Siofok, Hungary, June 6–8, pp. 1–10.
[6] Gailitis, A., and Lielausis, O., 1975, "Instability of Homogeneous Velocity Distribution in an Induction-Type MHD Machine," Magnetohydrodynamics, **11**(1), pp. 69–79.
[7] Kirillov, I. R., and Ostapenko, V. P., 1987, "Local Characteristics of a Cylindrical Induction Pump for Rm $s > 1$," Magnetohydrodynamics, **23**(2), pp. 196–202.
[8] Araseki, H., Kirillov, I. R., Preslitsky, G. V., and Ogorodnikov, A. P., 2000, "Double-Supply-Frequency Pressure Pulsation in Annular Linear Induction Pump—Part I: Measurement and Numerical Analysis," Nucl. Eng. Des., **195**(1), pp. 85–100.
[9] Araseki, H., Kirillov, I. R., Preslitsky, G. V., and Ogorodnikov, A. P., 2000, "Double-Supply-Frequency Pressure Pulsation in Annular Linear Induction Pump—Part II: Reduction of Pulsation by Linear Winding Grading at Both Stator Ends," Nucl. Eng. Des., **200**(3), pp. 397–406.
[10] Araseki, H., Kirillov, I. R., Preslitsky, G. V., and Ogorodnikov, A. P., 2004, "Magnetohydrodynamic Instability in Annular Linear Induction Pump—Part I: Experiment and Numerical Analysis," Nucl. Eng. Des., **227**(1), pp. 29–50.
[11] Araseki, H., Kirillov, I. R., Preslitsky, G. V., and Ogorodnikov, A. P., 2006, "Magnetohydrodynamic Instability in Annular Linear Induction Pump—Part II: Suppression of Instability by Phase Shift," Nucl. Eng. Des., **236**(9), pp. 965–974.
[12] Kirillov, I. R., and Obukhov, D. M., 2003, "Two Dimensional Model for Analysis of Cylindrical Linear Induction Pump Characteristics: Model Description and Numerical Analysis," Energy Convers. Manage., **44**(17), pp. 2687–2697.
[13] Kim, H. R., and Lee, Y. B., 2012, "MHD Stability Analysis of a Liquid Sodium Flow at the Annular Gap of an EM Pump," Ann. Nucl. Energy, **43**, pp. 8–12.
[14] Zhao, R., Li, H., and Zhang, D. S., 2018, "Numerical Investigation of Pump Performance and Internal Characteristics in ALIP With Different Winding Schemes," Int. J. Appl. Electromagn. Mech., **57**(3), pp. 1–13.
[15] Abdullina, K. I., Bogovalov, S. V., and Zaikov, Y. P., 2018, "3D Numerical Modeling of Liquid Metal Turbulent Flow in an Annular Linear Induction Pump," Ann. Nucl. Energy, **111**, pp. 118–126.
[16] Asada, T., Hirata, Y., Aizawa, R., Fujishima, Y., Suzuki, T., and Hoashi, E., 2015, "Development of a Three-Dimensional Magnetohydrodynamics Code for Electromagnetic Pumps," J. Nucl. Sci. Technol., **52**(5), pp. 633–640.
[17] Gissinger, C., Imazio, P. R., and Fauve, S., 2016, "Instability in Electromagnetically Driven Flows—I," Phys. Fluids, **28**(3), p. 034101.
[18] Roman, C., Dumont, M., Letout, S., Courtessole, C., Vitry, S., Rey, F., and Fautrelle, Y., 2014, "Modeling of Fully Coupled MHD Flows in Annular Linear Induction Pumps," Int. J. Appl. Electromagn. Mech., **44**(2), pp. 155–162.
[19] Biro, O., and Preis, K., 1989, "On the Use of the Magnetic Vector Potential in the Finite-Element Analysis of Three-Dimensional Eddy Currents," IEEE Trans. Magn., **25**(4), pp. 3145–3159.
[20] Abdullina, K. I., and Bogovalov, S. V., 2015, "3-D Numerical Modeling of MHD Flows in Variable Magnetic Field," Phys. Procedia, **72**, pp. 351–357.